HHS Public Access

Author manuscript

Pharm Res. Author manuscript; available in PMC 2017 October 01.

Published in final edited form as:

Pharm Res. 2016 October ; 33(10): 2400–2410. doi:10.1007/s11095-016-1963-8.

Design and Modular Construction of A Polymeric Nanoparticle for Targeted Atherosclerosis Positron Emission Tomography Imaging: A Story of 25% ^{64}Cu-CANF-Comb

Pamela K. Woodard[1], **Yongjian Liu**[1], **Eric D. Pressly**[2], **Hannah P. Luehmann**[1], **Lisa Detering**[1], **Deborah Sultan**[1], **Richard Laforest**[1], **Alaina J. McGrath**[2], **Robert J. Gropler**[1], and **Craig J. Hawker**[2,3,4]

[1]Department of Radiology, Washington University School of Medicine, St. Louis, MO

[2]Materials Research Laboratory, University of California, Santa Barbara, CA

[3]Department Chemistry and Biochemistry, University of California, Santa Barbara, CA

[4]Materials Department, University of California, Santa Barbara, CA

Abstract

Purpose—To assess the physicochemical properties, pharmacokinetic profiles, and *in vivo* positron emission tomography (PET) imaging of natriuretic peptide clearance receptors (NPRC) expressed on atherosclerotic plaque of a series of targeted, polymeric nanoparticles.

Methods—To control their structure, non-targeted and targeted polymeric (comb) nanoparticles, conjugated with various amounts of c-atrial natriuretic peptide (CANF, 0, 5, 10 and 25%), were synthesized by controlled and modular chemistry. *In vivo* pharmacokinetic evaluation of these nanoparticles was performed in wildtype (WT) C57BL/6 mice after ^{64}Cu radiolabeling. PET imaging was performed on an apolipoprotein E–deficient (ApoE$^{-/-}$) mouse atherosclerosis model to assess the NPRC targeting efficiency. For comparison, an *in vivo* blood metabolism study was carried out in WT mice.

Results—All three ^{64}Cu-CANF-comb nanoparticles showed improved biodistribution profiles, including significantly reduced accumulation in both liver and spleen, compared to the non-targeted ^{64}Cu-comb. Of the three nanoparticles, the 25% ^{64}Cu-CANF-comb demonstrated the best NPRC targeting specificity and sensitivity in ApoE$^{-/-}$ mice. Metabolism studies showed that the radiolabeled CANF-comb was stable in blood up to 9 days. Histopathological analyses confirmed the up-regulation of NPRC along the progression of atherosclerosis.

Conclusion—The 25% ^{64}Cu-CANF-comb demonstrated its potential as a PET imaging agent to detect atherosclerosis progression and status.

Corresponding author: Craig J. Hawker (hawker@mrl.ucsb.edu).
Pamela K. Woodard, Yongjian Liu, and Eric D. Pressly contributed equally to this work.

DISCLOSURES

No other potential conflict of interest relevant to this article was reported.

Keywords

Nanoparticle; Positron emission tomography; Atherosclerosis; Natriuretic peptide clearance receptor; Polymer Synthesis

INTRODUCTION

Over the past two decades, polymeric nanoparticles have been widely used in biomedical research, especially in the areas focusing on oncology, cardiology, pulmonology, inflammatory disease and drug delivery applications (1–6). Due to their unique size-related physicochemical properties, multivalent polymeric nanostructures are typically more efficient and efficacious than their monovalent counterparts both *in vitro* and *in vivo* (7–11). To date, most studies have focused on pre-clinical applications and a very limited number of polymeric nanostructures have ever been used in humans (12). Many challenges are associated with translational research, including the need for extensive preclinical studies, appropriate selection of clinical indications and proper design and successful completion of clinical trials. With these challenges in mind, it is critical that researchers fully understand the requirements of the translational process at the beginning of a project, especially designing and screening the appropriate agents for pre-clinical evaluation. Successful translational strategies can assist in bringing more nanopharmaceuticals from bench-top to patient bedside for clinical investigations.

Before beginning human clinical studies, researchers must submit an investigational new drug (IND) application for approval by the Food and Drug Administration. Polymeric nanoparticles are particularly attractive candidates for an IND application because their structure, and therefore resultant properties, can be accurately tuned and optimized by modular chemistry. This unique feature provides the flexibility to strategically modify the nanostructure size, morphology, composition, and surface properties in order to determine these features' effects on bioperformance. Rational selection of candidates for specific biomedical applications such as disease imaging or therapy can therefore be achieved (3, 13–16). Furthermore, modular, efficient and high yielding chemistry can help facilitate the large-scale and stringently-controlled synthesis of nanopharmaceuticals required for translational studies.

Atherosclerosis, the underlying basis of cardiovascular disease, is the leading cause of morbidity and mortality in Westernized societies. Typically characterized by the build-up of arterial plaque, atherosclerosis is associated with several phenotypes, including inflammation and thin fibrous cap formation during the longitudinal progression of the disease (17–19). Currently, most clinical diagnostic modalities used for atherosclerosis are anatomic in nature and provide limited information about plaque progression and activity. Some molecular agents, especially those that are radiolabeled, have shown promising ability to image biomarkers up-regulated on plaques by positron emission tomography (PET) or single photon emission computed tomography (SPECT) (11, 20–28). Unfortunately, clinical translation has usually been the bottleneck for validating these agents' ability to identify the stage and vulnerability of atherosclerotic plaques in humans. To get past this challenge, we

have invested ample work into identifying an appropriate biomarker and imaging system capable of detecting atherosclerotic plaques in pre-clinical models.

Natriuretic peptides are a family of heart- and vessel-derived hormones that play an important role in cardiovascular homeostasis by interacting with their corresponding natriuretic peptide receptors (NPRs). These receptors have been largely overlooked as potential targets for atherosclerosis imaging and therapy. Of the three NPRs, the clearance receptor (NPRC) has recently been demonstrated to be a biomarker for atherosclerosis in both animal models and human coronary arteries (29, 30). Therefore, we conjugated the NPRC binding peptide, C-type atrial natriuretic factor (CANF), to produce well-defined comb nanoparticles (CANF-comb) *via* controlled chemistry developed in our previous studies (15, 16, 31, 32). Herein, we demonstrate the effective design and modular construction of NPRC targeted comb nanoparticles for *in vitro* and *in vivo* evaluations. We compared the *in vivo* pharmacokinetics and PET plaque imaging efficiency of ^{64}Cu-CANF-combs conjugated with various amounts of CANF peptide in a mouse atherosclerosis model and identified the optimal candidate for human translational research.

MATERIALS & METHODS

Chemicals

Chemicals were purchased from Sigma-Aldrich (St. Louis, MO) and used without further purification unless stated. CANF peptide (98%, H-Arg-Ser-Ser-Cys-Phe-Gly-Gly-Arg-Ile-Asp-Arg-Ile-Gly-Ala-Cys-NH_2) was obtained from CPC Scientific (Sunnyvale, CA) by custom synthesis. Dioxopyrrolidin-1-yl pent-4-ynoate was purchased from Annova Chemical Inc (San Diego, CA), poly(ethylene glycol)-N_3 (PEG-N_3) from Nanocs Inc. (New York, NY), poly(ethylene glycol) monomethyl ether from Polymer Source (Dorval, QC, CAN) and 1,4,7,10-tetraazacyclododecane-1,4,7-tris(t-butyl acetate) (DOTA-*t*-Bu-ester) from Macrocyclics (Dallas, TX). Amicon Centriplus centrifugal filtration tubes (M_w cut-off = 30,000; 50,000) were purchased from Millipore (Billerica, MA). ^{64}Cu (half-life = 12.7 h, β^+ = 17%, β^- = 40%) was prepared on the Washington University Medical School CS-15 Cyclotron by the ^{64}Ni(p,n)^{64}Cu nuclear reaction at a specific activity of 1.85 GBq – 7.4 GBq/μg (end of bombardment), as previously described (33). 2,5-HiTrap Desalting columns (5 mL) were purchased from GE Healthcare Biosciences (Piscataway, NJ).

Instrumentation

Gel permeation chromatography (GPC) was carried out on a Waters (Millford, MA) chromatograph equipped with a Waters Alliance high pressure liquid chromatography (HPLC) system pump (2695 Separation Module) and four Visco Gel I-Series columns from Viscotek (dimensions = 7.8 mm × 30 cm). Detection was provided by a Waters 2414 differential refractometer and dimethyl formamide with 0.1 % LiBr was used as the mobile phase. Copolymer chromatograms were run at room temperature and calibrated to poly(methyl methacrylate) (PMMA) standards. Dynamic light scattering (DLS) was performed on a Wyatt Technology (Goleta, CA) DynaPro NanoStar™ at room temperature. Data was collected on 0.1 wt% aqueous nanoparticle solutions filtered through a 0.2 μm filter. Zeta potential measurements were acquired on a Malvern Zetasizer (Zetasizer Nano

ZS ZEN3600). A Bioscan 200 imaging scanner (Bioscan, Washington, DC) was used to read the instant thin layer chromatography (ITLC) plates (Pall ITLC-SG plates, VWR International, Batavia, IL). Fast protein liquid chromatography (FPLC) and radio-FPLC were performed using an ÄKTA FPLC system (GE Healthcare Biosciences) equipped with a Beckman 170 Radioisotope Detector (Beckman Instruments, Fullerton, CA). All other instrumentation can be found in our previous report (31).

Synthetic Procedures

General Considerations—Experimental procedures for the synthesis of *S*-methoxycarbonylphenylmethyl dithiobenzoate reversible addition-fragmentation chain-transfer (RAFT) agent (34); macro- and small molecule monomers, polyethylene glycol methacrylate (PEGMA), DOTA methacrylate (DOTA-MA) and CANF-PEG methacrylate (CANF-PEGMA); CANF-comb copolymers; and nanoparticles were adopted from previously published work with a few modifications (31).

Synthesis of CANF-Acetylene—Synthesis of CANF-acetylene was carried out as previously reported with the following modification: 2,5-Dioxopyrrolidin-1-yl pent-4-ynoate was used in the place of 4-pentynoic anhydride (31).

Synthesis of CANF Poly(Ethylene Glycol) Methacrylate (CANF-PEGMA)—Preparation of CANF-PEGMA was performed as previously reported with the following modification to the purification: The product was washed with a 0.01 M aqueous ethylenediaminetetraacetic acid (EDTA) solution containing 0.02 M NaOH (× 4) and Milli-Q water (× 10)(31).

Synthesis of CANF-Comb Copolymers—Synthesis of the comb copolymers was adopted from our previous work (31). To determine the influence of CANF incorporation on CANF-comb nanoparticle bioperformance *in vivo*, we focused on the synthesis of four copolymers. The series contains 0, 5, 10, and 25% CANF peptide conjugated to the PEG chains. 0% CANF serves as the non-targeted comb copolymer for control experiments. By using a controlled radical polymerization (RAFT), CANF peptide loading in the copolymer was dictated by the molar ratio of CANF-PEGMA to PEGMA.

Below is a representative example of the CANF-comb copolymer synthesis; in this example 25% of the PEG chains are conjugated with CANF peptides. PEGMA, 5.0 kDa (205 mg, 0.041 mmol), CANF-PEGMA 5.0 kDa (100 mg, 0.015 mmol), methyl methacrylate (MMA) (51.1 mg, 0.51 mmol), azobisisobutyronitrile (AIBN) (0.069 mg, 0.00042 mmol), DOTA-MA (22.2 mg, 0.032 mmol), and RAFT agent (0.33 mg, 0.0011 mmol) were added to a glass vial and dissolved in DMF (1.99 g). AIBN, DOTA-MA and the RAFT agent were all added to the vial as DMF stock solutions. The solution was transferred to a 5 mL Schlenk flask and degassed by three freeze-pump-thaw cycles followed by heating at 70 °C for 120 h. Following polymerization, the solution was diluted with DMF, transferred to four 15 mL Amicon Centriplus tubes (M_w cut-off = 50,000) and extensively washed with DMF until complete removal of monomers was observed by GPC. The copolymer was then washed

with MilliQ water (× 5) and freeze-dried to give the desired graft copolymer as a white powder (Yield 68 mg); M_n = 205 kDa, PDI = 1.20 (GPC-DMF, PMMA standards).

For the synthesis of the 10% CANF-comb copolymer, the amounts of PEGMA and CANF-PEGMA added in the reaction were 0.050 mmol and 0.006 mmol respectively; for 5%, the amounts were 0.053 mmol and 0.003 mmol. All other chemical amounts and reaction conditions were kept the same. The non-targeted comb copolymer (0% CANF) was synthesized with 0.056 mmols of PEGMA and no CANF-PEGMA monomer.

Formation of 0, 5, 10 and 25% CANF-Comb Nanoparticles—Deprotection and assembly of the 0, 5, 10 and 25% CANF-combs into nanoparticles were carried out as previously reported (31). A representative procedure follows: After deprotection of the DOTA groups, the freeze-dried comb copolymer was dissolved in DMSO (1 wt %) and heated to 50 °C until fully dissolved. The solution was cooled to room temperature and an equal volume of Milli-Q water was added all at once while stirring. To remove DMSO, the solution was transferred to 2 Amicon Centriplus (M_w cut-off = 30,000) centrifugal filtration tubes and concentrated and re-diluted with Milli-Q water until the DMSO content was less than 0.5 mg / mL by ^{1}H NMR. The resultant particles were characterized by DLS, re-diluted to 10 mg / mL and stored at −20 °C. The data for all particles are summarized in Table 1.

^{64}Cu Radiolabeling of CANF-Comb and Comb

The radiolabeling of CANF-comb and comb nanoparticles was adopted from our reported procedure (32). Briefly, the nanoparticles (5 μg, 5 pmol) were incubated with 185 MBq ^{64}Cu in 100 μL of a 0.1 M pH 5.5 ammonium acetate buffer at 80 °C for 1 h. After adding 5 μL EDTA (10 mM in 50 mM pH 7.4 phosphate buffer) to remove any non-specifically bound ^{64}Cu from the nanoparticles, the ^{64}Cu radiolabeled nanoparticles were separated from ^{64}Cu-EDTA with a 2 mL zeba spin desalting column. A 2 μL aliquot of the purified nanoparticles was spot on glass microfiber chromatography paper impregnated with silica gel and developed in a buffer composed of methanol and 10% ammonium acetate (volume ratio = 1:1). After separation, the radiochemical purity (RCP) of the ^{64}Cu radiolabeled nanoparticles was measured by radioactive thin layer chromatography (Radio-TLC) (Washington DC) to ensure the RCP was 95% or greater prior to *in vivo* studies.

Mouse Apolipoprotein E–Deficient (ApoE$^{-/-}$) Atherosclerosis Model

All animal studies were performed in compliance with guidelines set forth by the National Institutes of Health Office of Laboratory Animal Welfare and approved by the Washington University Animal Studies Committee. To assess the expression of the NPRC receptor and its connection with the development of plaque, a spontaneous apoE$^{-/-}$ mouse atherosclerosis model was developed for all PET imaging studies performed with the developed ^{64}Cu-CANF-comb nanoparticles. Basically, male, ApoE$^{-/-}$, 6 week old mice were fed a high cholesterol diet (HCD) (Harlan Teklad, 42% fat) to develop atherosclerotic plaque. To assess the longitudinal expression of the NPRC receptor and the imaging capability of the developed nanoparticles, mice were carried up to 38 weeks post HCD and PET imaging was conducted at early stage (18–26 weeks post HCD, average is 20 weeks) and late stage (32–

38 weeks post HCD, average is 35 weeks) of the plaque. Age-matched wildtype (WT) male C57BL/6 mice on normal chow were used as controls.

Bio-Distribution Studies

^{64}Cu-CANF-comb and comb nanoparticles were reconstituted in 0.9% sodium chloride (APP pharmaceuticals) for intravenous (i.v.) injection. Wild-type C57BL/6 mice weighing 25–32 g were anesthetized with inhaled isoflurane and injected with approximately 370 kBq of the radiolabeled nanoparticles (~ 4.0 μg/kg body weight) in 100 μL saline *via* tail vein. The mice were re-anesthetized before euthanizing by cervical dislocation at each time point (1 h, 4 h, and 24 h, n = 4/time point) post injection (p.i.). Organs of interest were collected, weighed and counted in a well gamma counter (Beckman 8000, San Diego, CA). Standards were prepared and measured along with the samples to calculate the percentage of the injected dose per gram of tissue (% ID/gram) or percentage of the injected dose per organ of tissue (%ID/organ) (35).

PET/CT Imaging

PET/CT imaging with 0, 5, 10 and 25% ^{64}Cu-CANF-combs was performed in ApoE$^{-/-}$ mice and the age-matched WT C57BL/6 analogue at the same time points with Inveon PET/CT (Siemens Healthcare). PET/CT scans were collected at 24 h post injection (p.i, 60 min static scan) and analyzed using the manufacturer's software (ASI Pro or IRW). The tracer uptake in the region of interest (ROI) was calculated as percent injected dose per gram of tissue (%ID/g) from the maximum a posteriori reconstructed images. After the last time point, the animals were euthanized by cervical dislocation and the aortic arches were either perfusion-fixed in situ with freshly prepared 4% paraformaldehyde in 1× PBS for histopathology and immunohistochemistry or fast frozen for RT-PCR analysis. To confirm the targeting specificity, competitive receptor blocking studies were also performed by co-injection of the ^{64}Cu radiolabeled CANF-comb candidate and corresponding non-radiolabeled CANF-comb in 100-fold excess (n = 6) followed by PET scans at 24 h p.i.

^{18}F-FDG PET/CT was also performed in the apoE$^{-/-}$ mice to compare with the data obtained with ^{64}Cu labeled nanoparticles. Mice were fasted for 4 h prior to the injection of ^{18}F-FDG (250 μCi in 100 μL saline) and the PET/CT scan was performed at 1 h p.i.

Blood metabolism study

To assess the stability of radiolabeled CANF-comb and chemical components present at region of interest on the related PET image, longitudinal blood metabolism of 25% CANF-comb was performed *via* ^{67}Cu radiolabeling, due to its long half-life ($t_{1/2}$= 61.8 h) compared to ^{64}Cu ($t_{1/2}$= 12.7 h). After intravenous injection in C57BL/6 mice (444 kBq/mouse, n = 60), blood was collected into syringes containing acid citrate dextrose at 1, 2, 5, 7, 9 and 12 days post injection and subjected to centrifugation (200 g for 15 min and then 1000 g for 10 min) to separate whole blood, platelet rich plasma, platelet poor plasma and platelet pellet. The platelet poor plasma fraction was injected into GE AKTA FPLC system equipped with a UV detector, a flow count radioactivity detector (Bioscan) and fraction collector Frac-920. The separation was performed on Superose-12 10/300 size exclusion column and eluted with

SEC buffer at a flow rate of 0.8 mL/min. The fractions were collected every minute and counted in a gamma counter (PerkinElmer Wizard 3 gamma counter).

Octanol–Water Partition Coefficient Measurement

About 370 kBq of ^{64}Cu labeled nanoparticles in 500 μL of saline were added to 500 μL of octanol in an Eppendorf microcentrifuge tube (Brinkman). The 2 layers were mixed for 10 min at room temperature, the tube was centrifuged at 14,000 rpm for 5 min (model 5415C Eppendorf microcentrifuge, Brinkman), and the counts in 100 μL aliquots of both organic and inorganic layers were determined by use of a γ-counter (Packard). The experiment was repeated 3 times (36).

Immunohistochemistry

After radioactivity decay, animal tissue specimens were fixed in 4% paraformaldehyde immediately after collection, stored overnight at 4 °C, and embedded in paraffin and sectioned at 5 microns for immunohistochemistry. Following de-waxing and hydration, sections were heated in 10 mM sodium citrate (pH 6.0) with 0.1% Tween for 15 minutes at boiling temperature for antigen retrieval. Following blocking with non-immune serum, sections were incubated with Genway (San Diego, CA) mouse monoclonal anti-NPRC antibody 4 °C overnight at 1:400 dilution using Vector Laboratories M.O.M. kit (Burlingame, CA). Color development employed Vector Laboratories Vectastain alkaline phosphatase ABC system (Burlingame, CA) and blue substrate, and sections were counterstained using nuclear fast red. Sections incubated with pre-immune serum, and sections incubated with secondary antibody only, gave no signal.

Statistical Analysis

Group variation is described as the mean ± standard deviation. Group comparisons were made using the student t-test. The significance level in all tests was $p \leq 0.05$. GraphPad Prism v. 6.04 (La Jolla, CA) was used for all statistical analyses.

RESULTS AND DISCUSSION

Synthesis of 0, 5%, 10%, and 25% CANF-comb nanoparticles

To systematically study the influence of CANF peptide incorporation on *in vivo* pharmacokinetics and PET imaging efficiency, we focused on the synthesis of four comb nanoparticles, each with a different peptide loading. The nanoparticle series was synthesized by adopting the modular strategy previously developed, where precise control over the number and location of CANF in the final assembled structure could be accomplished (15, 16, 32). First, comb copolymers were prepared by employing three functional methacrylate-based monomers: PEG-methacrylate (PEGMA), CANF-PEG-methacrylate (CANF-PEGMA), and DOTA-methacrylate (DOTA-MA). Each monomer was designed to give the resultant copolymer and final assembled nanostructure specific properties. For example, the hydrophilic PEG groups imparted biocompatibility and when incorporated in the right ratio with the PMMA backbone, drove assembly of the polymers into star-like nanoparticles (16). In addition, incorporation of CANF peptides and DOTA ligands enabled NPRC targeting and PET imaging, respectively. These functional monomers were randomly copolymerized

with methyl methacrylate *via* reversible RAFT polymerization to achieve the amphiphilic comb copolymer depicted in figure 1a. By using a controlled radical polymerization technique, the feed ratio of the functional monomers dictated the ratio incorporated into the final copolymer. Importantly, this allowed us to dial in specific peptide quantities (0 to 25%, referring to the percent CANF peptide conjugated to the PEG chains, Fig. 1b) in order to optimize the final nanoparticle efficiency for targeting NPRC. In addition to functional group incorporation, control over total molecular weight and dispersity was also achieved. Assembly of the comb copolymers was accomplished as previously reported (16, 31), resulting in star-like nanoparticles dispersed in water. The diameters of these nanoparticles were comparable (16–22 nm range) within the 0–25% CANF-comb series, which was consistent with our previous results (15). Finally, ^{64}Cu radiolabels were introduced into the nanoparticles via DOTA chelation. All comb nanoparticles within the series had comparable specific activities, confirming that we had controlled the number of DOTA groups incorporated into the comb copolymers before assembly (Table 1). Due to the achieved control over nanoparticle functionality and size, a systematic study on the influence of CANF loading on pharmacokinetics and PET imaging efficiency was carried out.

In vivo Pharmacokinetics of ^{64}Cu-CANF-Combs and ^{64}Cu-Comb

First, biodistribution profiles of the ^{64}Cu-CANF-comb nanoparticle series in wild type (WT) mice were acquired and evaluated. Initially we compared the non-targeted ^{64}Cu-comb (control particle) with the 25% ^{64}Cu-CANF-comb (particles with the highest peptide incorporation), anticipating that these samples would show the biggest differences. In contrast to the 25% ^{64}Cu-CANF-combs, the non-targeted ^{64}Cu-comb showed comparable blood pool (blood, lung and heart) retention at all three time points (Fig. 2). Even though there was no CANF conjugated to it, the non-targeted ^{64}Cu-comb's mononuclear phagocyte system (MPS) accumulations, including liver and spleen, were all 4–5 fold ($p<0.0001$, $n=4$) higher than those acquired with 25% ^{64}Cu-CANF-combs during the 24 h study. We attribute this phenomenon to the difference in nanoparticle surface charge as we reported previously (31, 32). The other two ^{64}Cu-CANF-combs (5% and 10%), which had a difference of approximately 7 CANF peptides conjugated, showed similar biodistribution profiles in all major organs collected during the 24 h study including the blood retention half-lives ($t_{1/2}$= 8.8 h and 8.9 h for 5% and 10%, respectively). Specifically, they both showed high initial blood retention (> 45%ID/g at 1 h p.i.), which decreased slightly to > 40%ID/g at 4h, and 22% at 24 h p.i. These extended blood circulations are consistent with our previous report, which showed increased circulation time with increasing PEG chain length. In this study all nanoparticles contain the largest PEG length from our previous study (5 kDa). Furthermore, the blood retentions of 5%, and 10% were both two times that obtained for 25% ^{64}Cu-CANF-comb ($p <0.0001$, $n=4$). Since all CANF-comb nanoparticles were neutrally charged, the difference in blood circulation could be related to variation in hydrophobicity. To determine this, we measured the octanol-water partition coefficient (log p) for each nanoparticle, as shown in Table 1. It was found that with increased CANF conjugation, log p also increased, with the largest increase observed upon going from 10 to 25% peptide. These results implied an increase in hydrophobicity with CANF conjugation and aligned with our hypothesis about blood circulation. In addition, the three CANF-combs had comparable retentions in the liver and spleen at each time point during the 24 h study. Due to the

inherent polydispersity of the synthesized nanoparticles or the transchelation of ^{64}Cu from DOTA by serum protein (37, 38), renal clearance through the kidneys (< 12%ID/g at all time points) was observed for all the four nanoparticles, with the non-targeted ^{64}Cu-comb having slightly higher retention. The three targeted ^{64}Cu-CANF-combs had significantly lower liver and spleen retention than the non-targeted ^{64}Cu-comb at each time point measured, suggesting retention of these nanoparticles in other organs or excretion through feces. The three ^{64}Cu-CANF-combs all had comparable liver and spleen retentions.

PET Imaging in Mouse ApoE$^{-/-}$ Atherosclerosis Model

In the apoE$^{-/-}$ mouse atherosclerosis model, PET/CT imaging was performed on early stage plaque (~20 weeks post HCD) for the four nanoparticle series. Consistent with the biodistribution studies, both the 5% and 10% ^{64}Cu-CANF-combs showed high PET intensity in blood pool organs, including the heart, lungs, and blood vessels, even at 24 h p.i. Quantitative analysis showed that the accumulations of 5% and 10% ^{64}Cu-CANF-combs at aortic arches of apoE$^{-/-}$ mice were 6.2 ± 1.2%ID/g and 6.0 ± 0.9%ID/g (n=4/group for both), respectively; however, the long blood circulation of these two nanoparticles resulted in high accumulations in the aortic arches of WT mice (4.8 ± 1.1%ID/g and 4.6 ± 1.0%ID/g for 5% and 10%, respectively, n=4/group) as well. Since similar accumulations were observed in the apoE$^{-/-}$ and WT mice, the 5% and 10% ^{64}Cu-CANF-combs are less favorable PET agents for imaging plaque by specific biomarkers. As expected, the non-targeted ^{64}Cu-comb had non-specific retention in the aortic arch of apoE$^{-/-}$ mice (2.6 ± 0.5%ID/g (n=4/group).

In contrast to the 5 and 10% ^{64}Cu-CANF-comb, the 25% analogue had lower blood retention, which resulted in lower uptake at the aortic arch in WT mice (2.6 ± 0.6 %ID/g (n=4/group) at 24 h p.i.). This value was approximately half of that obtained with 5% and 10% ^{64}Cu-CANF-comb. PET/CT imaging of ApoE$^{-/-}$ mice with early stage plaque showed significant accumulation of radioactivity at the aortic arch (Fig. 3a). Quantitative uptake analysis showed that the tracer localization of 25% ^{64}Cu-CANF-comb at the aortic arch was 8.8 ± 0.8 %ID/g (n=6/group), which was 2.3 times ($p < 0.0001$) higher than that acquired from WT mice (Fig. 3b). For the non-targeted ^{64}Cu-comb, the retentions in the aortic arch of apoE$^{-/-}$ mice was 2.4 ± 0.4 %ID/g (n=4/group), significantly ($p < 0.0001$) lower than the targeted counterpart. Given that ^{64}Cu-comb and 25% ^{64}Cu-CANF-comb had similar blood retention in the biodistribution studies (Fig. 2), and if we consider the accumulation of ^{64}Cu-comb at plaque as non-specific background retention (that will be subtracted from the uptake of its targeted counterpart), approximately 73% of the PET signal at the atherosclerotic plaque was due to NPRC receptor mediated uptake.

For late stage plaque, both the uptake of 25% ^{64}Cu-CANF-comb (7.5 ± 0.7 %ID/g, n=6/group) and ^{64}Cu-Comb (1.8 ± 0.3 %ID/g, n=4/group) decreased slightly compared to values measured for earlier stage plaque (20 weeks post HCD). One possible explanation is the reduction in non-specific retention of both nanoparticles at the aortic arch due to the narrowed lumen that occurs with disease progression (Fig. 4). Following the same calculation discussed above, the retention of 25% ^{64}Cu-CANF-comb at plaque was actually increased to 76% positivity for the NPRC receptor. In the age-matched WT mice, the

accumulation (2.1 ± 0.2 %ID/g, n=4/group) of 25% ^{64}Cu-CANF-comb at the aortic arch was comparable to the results obtained for early stage plaque.

During this longitudinal study, the uptake of ^{18}F-FDG at the aortic arch during early (2.6 ± 0.6 %ID/g, n=4/group) and late stages (2.2 ± 0.8 %ID/g, n=4/group) of plaque formation was also investigated. Uptake at both stages of plaque were significantly ($p < 0.0001$ for both) lower than those acquired with 25% ^{64}Cu-CANF-comb. Furthermore, when compared to other reported nanoparticles used for plaque imaging in spontaneous apoE$^{-/-}$ mouse model (22, 39), the 25% ^{64}Cu-CANF-comb showed more accurate and specific detection of biomarkers upregulated on plaque at multiple time points during the progression of disease. This indicates that the NPRC targeted nanoparticle has great potential to track the progression of atherosclerosis via PET imaging.

Competitive receptor blocking studies were also carried out to demonstrate the targeting specificity. As shown in figure 4, tracer uptake at the aortic arch was significantly decreased to a level (2.7 ± 0.8 %ID/g, n=4/group) comparable to that obtained with non-targeted ^{64}Cu-Comb, confirming the NPRC receptor mediated uptake at atherosclerotic plaque.

Histology and Immunohistochemistry

In contrast to the results obtained from WT mice, the representative hematoxyline and eosin (H&E) staining of aortic arches harvested from apoE$^{-/-}$ mice at 24 and 36 weeks post HCD demonstrated significant progression of plaque with atherosclerosis characteristics, including neointima thickening and foam cell infiltration (Fig. 4). Compared to 24 weeks, the plaque at 35 weeks was more amorphous, less cellular and filled with lipid crystals throughout the neointima. The image J analysis of plaques showed that the nuclei count per pixel of plaque at 36 weeks was 3.5 times less than that at 24 weeks, which was consistent with our previous report in a rabbit atherosclerosis model (30).

Immunohistochemistry of the apoE$^{-/-}$ mouse aortic arch depicted the up-regulation of NPRC receptors throughout the plaque during late stage atherosclerosis, including dense expression in media, intima, and the surface of plaque (Fig. 5). Apart from smooth muscle cells and endothelial cells as we previously reported (30, 32), most of the inflammatory cells on the plaque surface were positive for NPRC, indicating the great potential of this receptor as a biomarker for atherosclerosis. More importantly, the overexpression of NPRC on plaque was consistent with the high uptake of 25% ^{64}Cu-CANF-comb through PET imaging. If we take into account the decreased cellularity with the progression of plaque, the 25% ^{64}Cu-CANF-comb uptake per pixel of late stage plaque was actually tripled compared to the data acquired at 20 weeks post HCD. This demonstrated that 25% ^{64}Cu-CANF-comb has great potential as a PET tracer for sensitive and specific detection of atherosclerotic plaque and tracking the progression of disease.

Blood metabolism study

To assess the *in vivo* stability and metabolism in blood, the 25% CANF-comb was radiolabeled with ^{67}Cu for a longitudinal study in WT mice. Blood samples were collected from mice and centrifuged to separate cells and plasma. Gamma counting analysis showed that 97.3 ± 1.0% of radioactivity was in plasma with only 2.7± 0.9% associated with red

blood cells. Further analysis of platelet rich and poor plasma showed no significant difference, indicating that ^{67}Cu-CANF-comb had no preferential binding for platelets. As shown in figure 6, the FPLC profiles indicated that the radiolabeled 25% ^{67}Cu-CANF-comb was stable in blood for up to 9 days. At day 12, a notable peak was observed next to the 25% ^{67}Cu-CANF-comb peak, which we believe was either due to degradation of the CANF-comb nanoparticle or transchelation of ^{67}Cu from DOTA by serum proteins such as ceruloplasmin. In contrast to the nanostructure with DOTA conjugated on the surface (38), the CANF-comb design with DOTA collapsed in the hydrophobic core demonstrated its advantage in improving radiolabel stability for accurate detection of biomarkers to track progression or status of disease. It should be noted that the FPLC profiles were based on gamma counting of ^{67}Cu, not UV absorption of nanoparticles, due to interference from serum proteins. The degradation of small component of CANF-comb may not be detectable by UV.

CONCLUSIONS

The modular design and construction of a series of NPRC targeted comb nanoparticles was exploited to evaluate their ability to image atherosclerosis via PET/CT imaging in a mouse apoE$^{-/-}$ model. Pharmacokinetic assessment of the series showed that the 25% ^{64}Cu-CANF-comb had the lowest blood retention, which resulted in a higher net PET signal at atherosclerotic plaques. In addition, the impressive sensitivity and targeting specificity of 25% ^{64}Cu-CANF-comb can be attributed to efficient binding to up-regulated NPRC located on atherosclerotic plaques, determined by immunohistochemistry. The biological confirmation of previous PET imaging results demonstrates that this nanoparticle has significant potential to be a successful, noninvasive approach to further assess the pathological function of NPRC during the progression of atherosclerotic plaque development and provides useful information about its vulnerability.

Acknowledgments

This work is supported by the National Heart, Lung and Blood Institute of the National Institutes of Health as a Program of Excellence in Nanotechnology (HHSN268201000046C). The characterization of nanoparticles was performed in the Central Facilities of the UCSB Materials Research Laboratory supported by the MRSEC Program of the National Science Foundation under award no. DMR1121053.

We thank Nicole Fettig, Margaret Morris, Amanda Roth, Lori Strong, and Ann Stroncek for their assistance with animals and imaging studies and Tom Voller, Evelyn Madrid, Paul Eisenbies, Efrem Mebrahtu, and Suzanne Lapi for ^{64}Cu production. We thank the helpful discussion and comments from Dr. Richard Pierce.

ABBREVIATIONS

°C	Degree Celsius
%ID/g	Percent injected dose per gram of tissue
%ID/organ	Percent injected dose per organ of tissue
^{18}F-FDG	2-deoxy-2-[18F]-fluoro-D-glucose
AIBN	Azobisisobutyronitrile

ApoE$^{-/-}$	Apolipoprotein E-deficient
CANF	C-type atrial natriuretic factor
DLS	Dynamic light scattering
DMF	N, N-Dimethylformamide
DOTA	1,4,7,10-tetraazacyclododecane-1,4,7-tris(t-butyl acetate)
EDTA	Ethylenediaminetetraacetic acid
FIG	Figure
FPLC	Fast performance liquid chromatography
GPC	Gel permeation chromatography
HCD	High cholesterol diet
H&E	Hematoxyline and eosin
HPLC	High pressure liquid chromatography
IND	Investigational new drug
ITLC	Instant thin layer chromatography
I.V.	Intravenous
MPS	Mononuclear phagocyte system
NPRs	Natriuretic peptide receptors
NPRC	Natriuretic peptide clearance receptor
PDI	Polydispersity index
PEGMA	Polyethylene glycol methacrylate
PET/CT	Positron emission tomography/Computed tomography
PI	Post injection
PMMA	Poly(methyl methacrylate)
RAFT	Reversible addition-fragmentation chain-transfer
RCP	Radiochemical purity
SPECT	Single photon emission computed tomography
WT	Wildtype

References

1. Nicolas J, Mura S, Brambilla D, Mackiewicz N, Couvreur P. Design, functionalization strategies and biomedical applications of targeted biodegradable/biocompatible polymer-based nanocarriers for drug delivery. Chem Soc Rev. 2013; 42(3):1147–1235. [PubMed: 23238558]
2. Yang X, Yang M, Pang B, Vara M, Xia Y. Gold Nanomaterials at Work in Biomedicine. Chem Rev. 2015; 115(19):10410–10488. [PubMed: 26293344]
3. Elsabahy M, Heo GS, Lim SM, Sun G, Wooley KL. Polymeric Nanostructures for Imaging and Therapy. Chem Rev. 2015; 115(19):10967–11011. [PubMed: 26463640]
4. Serra P, Santamaria P. Nanoparticle-based autoimmune disease therapy. Clin Immunol. 2015; 160(1):3–13. [PubMed: 25704658]
5. Andrade F, Rafael D, Videira M, Ferreira D, Sosnik A, Sarmento B. Nanotechnology and pulmonary delivery to overcome resistance in infectious diseases. Adv Drug Deliv Rev. 2013; 65(13–14):1816–1827. [PubMed: 23932923]
6. Omlor AJ, Nguyen J, Bals R, Dinh QT. Nanotechnology in respiratory medicine. Respir Res. 2015; 16:64. [PubMed: 26021823]
7. Kemp JA, Shim MS, Heo CY, Kwon YJ. "Combo" nanomedicine: Co-delivery of multi-modal therapeutics for efficient, targeted, and safe cancer therapy. Adv Drug Deliv Rev. 2016; 98:3–18. [PubMed: 26546465]
8. Young SW, Stenzel M, Jia-Lin Y. Nanoparticle-siRNA: A potential cancer therapy? Crit Rev Oncol Hematol. 2016; 98:159–169. [PubMed: 26597018]
9. Yang Y, Yu C. Advances in silica based nanoparticles for targeted cancer therapy. Nanomedicine. 2016; 12(2):317–332. [PubMed: 26706409]
10. Hofferberth SC, Grinstaff MW, Colson YL. Nanotechnology applications in thoracic surgery. Eur J Cardiothorac Surg. 2016
11. Stendahl JC, Sinusas AJ. Nanoparticles for Cardiovascular Imaging and Therapeutic Delivery, Part 2: Radiolabeled Probes. J Nucl Med. 2015; 56(11):1637–1641. [PubMed: 26294304]
12. Min Y, Caster JM, Eblan MJ, Wang AZ. Clinical Translation of Nanomedicine. Chem Rev. 2015; 115(19):11147–11190. [PubMed: 26088284]
13. Welch MJ, Hawker CJ, Wooley KL. The advantages of nanoparticles for PET. J Nucl Med. 2009; 50(11):1743–1746. [PubMed: 19837751]
14. Elsabahy M, Wooley KL. Design of polymeric nanoparticles for biomedical delivery applications. Chem Soc Rev. 2012; 41(7):2545–2561. [PubMed: 22334259]
15. Shokeen M, Pressly ED, Hagooly A, Zheleznyak A, Ramos N, Fiamengo AL, Welch MJ, Hawker CJ, Anderson CJ. Evaluation of Multivalent, Functional Polymeric Nanoparticles for Imaging Applications. ACS Nano. 2011; 5(2):738–747. [PubMed: 21275414]
16. Pressly ED, Rossin R, Hagooly A, Fukukawa K-I, Messmore BW, Welch MJ, Wooley KL, Lamm MS, Hule RA, Pochan DJ, Hawker CJ. Structural Effects on the Biodistribution and Positron Emission Tomography (PET) Imaging of Well-Defined 64Cu-Labeled Nanoparticles Comprised of Amphiphilic Block Graft Copolymers. Biomacromolecules. 2007; 8(10):3126–3134. [PubMed: 17880180]
17. Sanz J, Fayad ZA. Imaging of atherosclerotic cardiovascular disease. Nature. 2008; 451(7181): 953–957. [PubMed: 18288186]
18. Libby P, Ridker PM, Hansson GK. Progress and challenges in translating the biology of atherosclerosis. Nature. 2011; 473(7347):317–325. [PubMed: 21593864]
19. Libby P. Inflammation in atherosclerosis. Arterioscler Thromb Vasc Biol. 2012; 32(9):2045–2051. [PubMed: 22895665]
20. Liu Y, Welch MJ. Nanoparticles labeled with positron emitting nuclides: advantages, methods, and applications. Bioconjug Chem. 2012; 23(4):671–682. [PubMed: 22242601]
21. Magnoni M, Ammirati E, Camici PG. Non-invasive molecular imaging of vulnerable atherosclerotic plaques. J Cardiol. 2015; 65(4):261–269. [PubMed: 25702846]

22. Nahrendorf M, Zhang H, Hembrador S, Panizzi P, Sosnovik DE, Aikawa E, Libby P, Swirski FK, Weissleder R. Nanoparticle PET-CT imaging of macrophages in inflammatory atherosclerosis. Circulation. 2008; 117(3):379–387. [PubMed: 18158358]
23. Sadat U, Jaffer FA, van Zandvoort MA, Nicholls SJ, Ribatti D, Gillard JH. Inflammation and neovascularization intertwined in atherosclerosis: imaging of structural and molecular imaging targets. Circulation. 2014; 130(9):786–794. [PubMed: 25156914]
24. Stacy MR, Sinusas AJ. Novel Applications of Radionuclide Imaging in Peripheral Vascular Disease. Cardiol Clin. 2016; 34(1):167–177. [PubMed: 26590787]
25. Stendahl JC, Sinusas AJ. Nanoparticles for Cardiovascular Imaging and Therapeutic Delivery, Part 1: Compositions and Features. J Nucl Med. 2015; 56(10):1469–1475. [PubMed: 26272808]
26. Tarkin JM, Joshi FR, Rajani NK, Rudd JH. PET imaging of atherosclerosis. Future Cardiol. 2015; 11(1):115–131. [PubMed: 25606707]
27. Tarkin JM, Joshi FR, Rudd JH. PET imaging of inflammation in atherosclerosis. Nat Rev Cardiol. 2014; 11(8):443–457. [PubMed: 24913061]
28. Irkle A, Vesey AT, Lewis DY, Skepper JN, Bird JL, Dweck MR, Joshi FR, Gallagher FA, Warburton EA, Bennett MR, Brindle KM, Newby DE, Rudd JH, Davenport AP. Identifying active vascular microcalcification by (18)F-sodium fluoride positron emission tomography. Nat Commun. 2015; 6:7495. [PubMed: 26151378]
29. Casco VH, Veinot JP, Kuroski de Bold ML, Masters RG, Stevenson MM, de Bold AJ. Natriuretic peptide system gene expression in human coronary arteries. J Histochem Cytochem. 2002; 50(6): 799–809. [PubMed: 12019296]
30. Liu Y, Abendschein D, Woodard GE, Rossin R, McCommis K, Zheng J, Welch MJ, Woodard PK. Molecular imaging of atherosclerotic plaque with 64Cu-labeled natriuretic peptide and PET. J Nucl Med. 2010; 51(1):85–91. [PubMed: 20008978]
31. Pressly ED, Pierce RA, Connal LA, Hawker CJ, Liu Y. Nanoparticle PET/CT imaging of natriuretic peptide clearance receptor in prostate cancer. Bioconjugate chemistry. 2013; 24(2):196–204. [PubMed: 23272904]
32. Liu Y, Pressly ED, Abendschein DR, Hawker CJ, Woodard GE, Woodard PK, Welch MJ. Targeting angiogenesis using a C-type atrial natriuretic factor-conjugated nanoprobe and PET. J Nucl Med. 2011; 52(12):1956–1963. [PubMed: 22049461]
33. Liu Y, Pierce R, Luehmann HP, Sharp TL, Welch MJ. PET imaging of chemokine receptors in vascular injury-accelerated atherosclerosis. J Nucl Med. 2013; 54(7):1135–1141. [PubMed: 23658218]
34. Perrier S, Takolpuckdee P, Westwood J, Lewis DM. Versatile Chain Transfer Agents for Reversible Addition Fragmentation Chain Transfer (RAFT) Polymerization to Synthesize Functional Polymeric Architectures. Macromolecules. 2004; 37(8):2709–2717.
35. Liu Y, Ibricevic A, Cohen JA, Cohen JL, Gunsten SP, Frechet JM, Walter MJ, Welch MJ, Brody SL. Impact of hydrogel nanoparticle size and functionalization on in vivo behavior for lung imaging and therapeutics. Mol Pharm. 2009; 6(6):1891–1902. [PubMed: 19852512]
36. Chen X, Hou Y, Tohme M, Park R, Khankaldyyan V, Gonzales-Gomez I, Bading JR, Laug WE, Conti PS. Pegylated Arg-Gly-Asp peptide: 64Cu labeling and PET imaging of brain tumor alphavbeta3-integrin expression. J Nucl Med. 2004; 45(10):1776–1783. [PubMed: 15471848]
37. Boswell CA, Sun X, Niu W, Weisman GR, Wong EH, Rheingold AL, Anderson CJ. Comparative in vivo stability of copper-64-labeled cross-bridged and conventional tetraazamacrocyclic complexes. J Med Chem. 2004; 47(6):1465–1474. [PubMed: 14998334]
38. Wang Y, Liu Y, Luehmann H, Xia X, Brown P, Jarreau C, Welch M, Xia Y. Evaluating the pharmacokinetics and in vivo cancer targeting capability of Au nanocages by positron emission tomography imaging. ACS Nano. 2012; 6(7):5880–5888. [PubMed: 22690722]
39. Majmudar MD, Yoo J, Keliher EJ, Truelove JJ, Iwamoto Y, Sena B, Dutta P, Borodovsky A, Fitzgerald K, Di Carli MF, Libby P, Anderson DG, Swirski FK, Weissleder R, Nahrendorf M. Polymeric nanoparticle PET/MR imaging allows macrophage detection in atherosclerotic plaques. Circ Res. 2013; 112(5):755–761. [PubMed: 23300273]

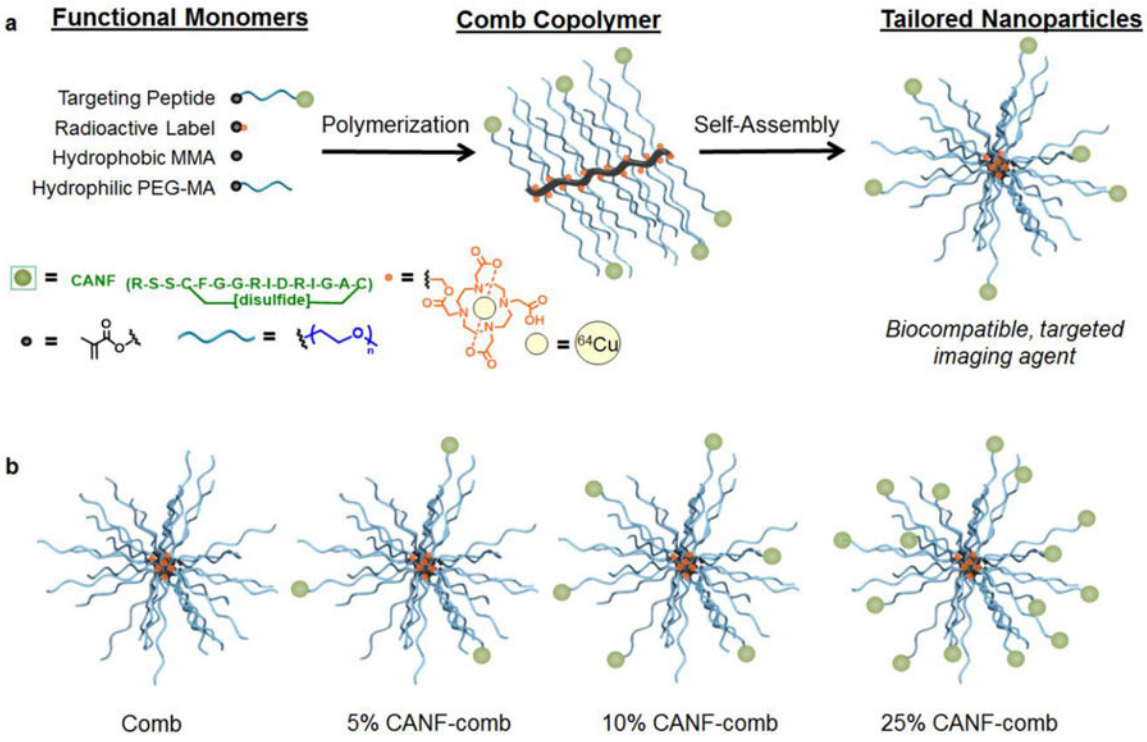

Fig. 1.

a) Modular design of targeted, nanoscale imaging agents for early-stage disease detection and b) cartoon representation of tailored nanoparticles with 5, 10 and 25% CANF loading. Percentages refer to the feed ratio of the CANF-PEG monomers relative to the total PEG monomers.

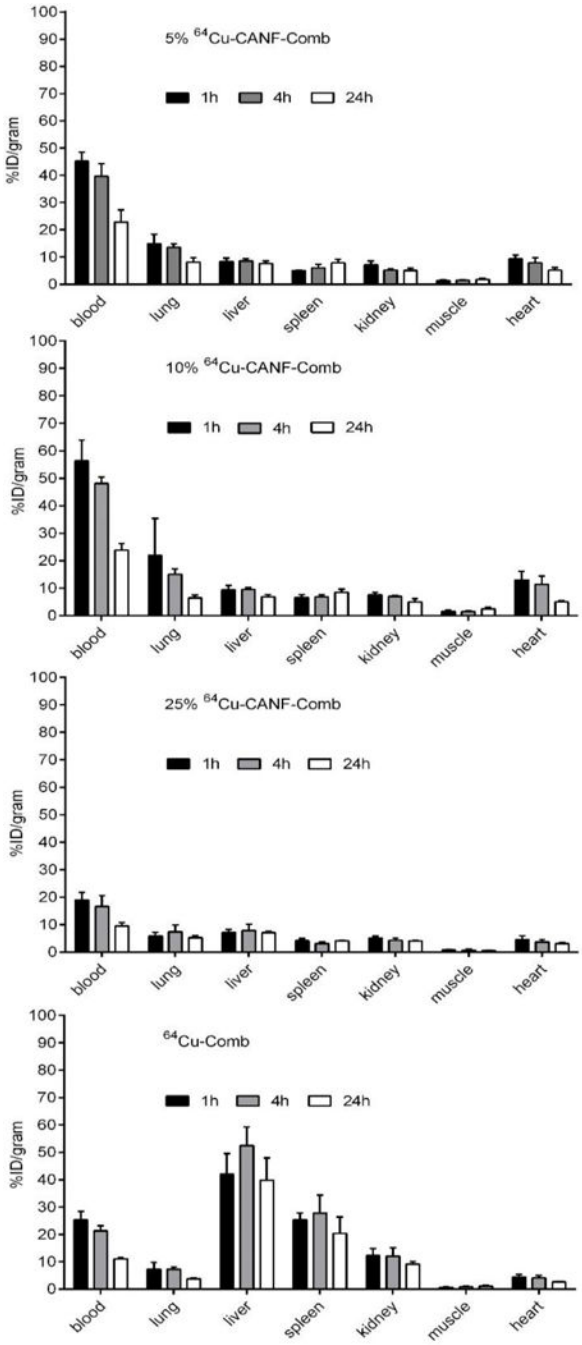

Fig. 2.

Biodistribution of 5%, 10%, 25% ^{64}Cu-CANF-Comb and ^{64}Cu-comb in wildtype mice at 1h, 4h, and 24h post intravenous injection through tail vein (n=4/group). The data of 10%, 25% ^{64}Cu-CANF-Comb and ^{64}Cu-comb were previously reported in reference 31 and 32.

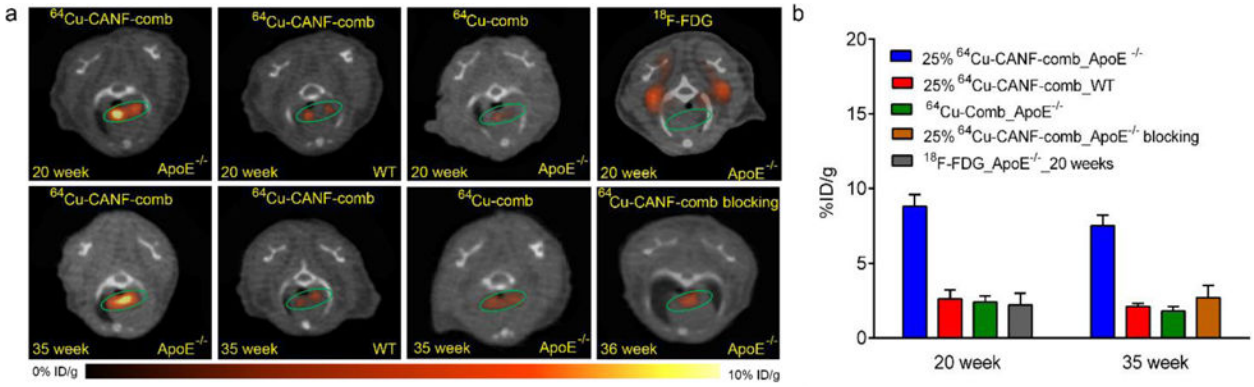

Fig. 3.

a) Representative PET/CT images (transverse plane) of 25% ^{64}Cu-CANF-Comb, ^{64}Cu-comb and ^{18}F-FDG in apoE$^{-/-}$ mice at 20 weeks and 35 weeks post HCD. Green circle: aortic arch b) Quantitative uptake analysis of 25% ^{64}Cu-CANF-comb and ^{64}Cu-comb and ^{18}F-FDG at aortic arches during the progression of atherosclerosis.

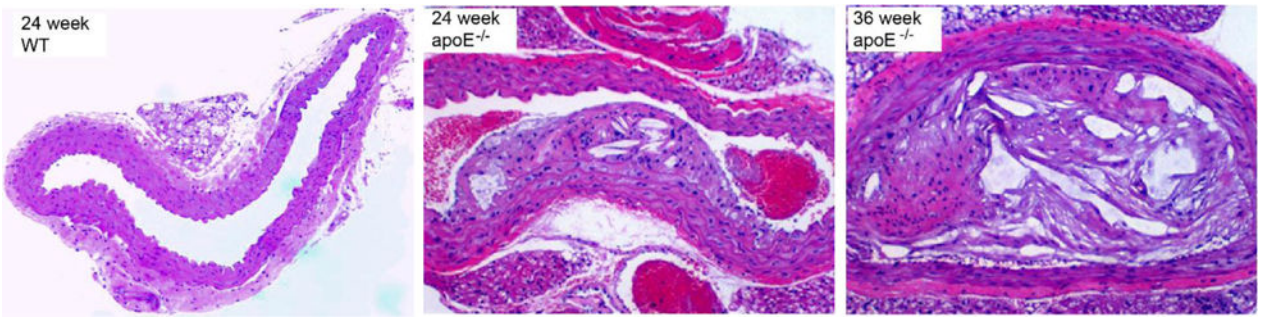

Fig. 4.

H&E staining of aortic arches of WT and apoE$^{-/-}$ mice at 24 and 36 weeks post HCD showing the progression of plaque.

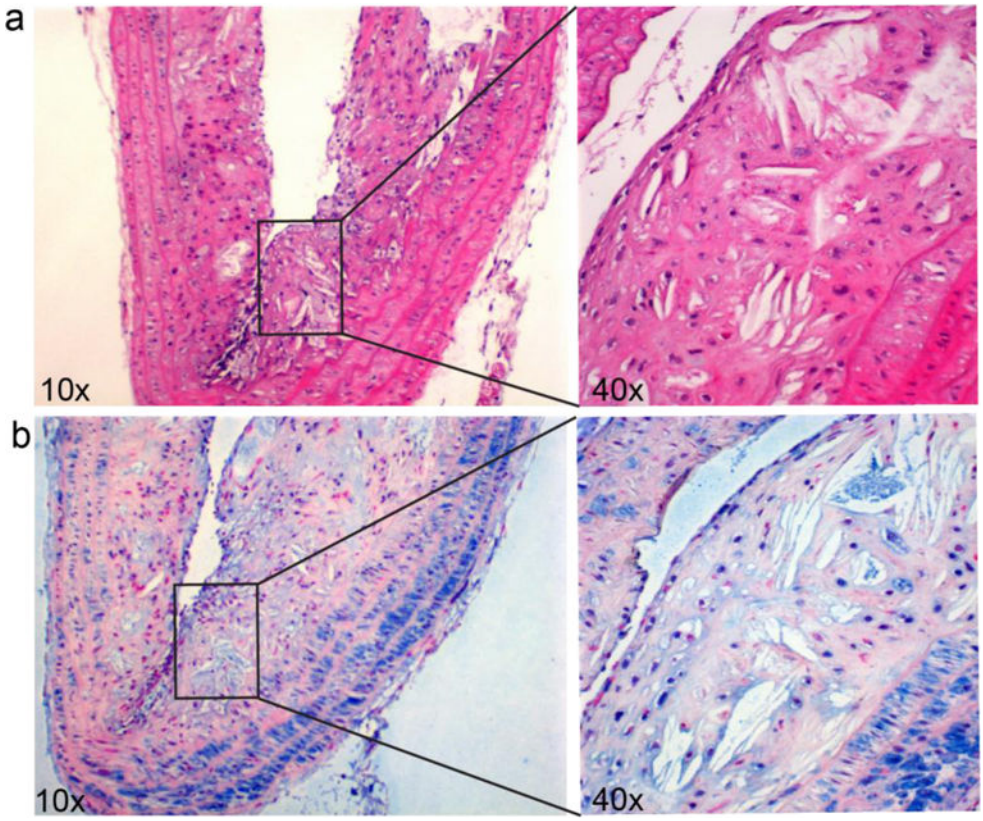

Fig. 5.

H&E staining (a) and immunohistochemistry of NPRC receptor (b) in apoE$^{-/-}$mouse aortic arch at 36 weeks post HCD. H&E showed the significant and complex development of plaque. Immunohistochemistry showed the significant overexpression of NPRC receptor (blue) across the plaque from media, neointima and the surface of plaque.

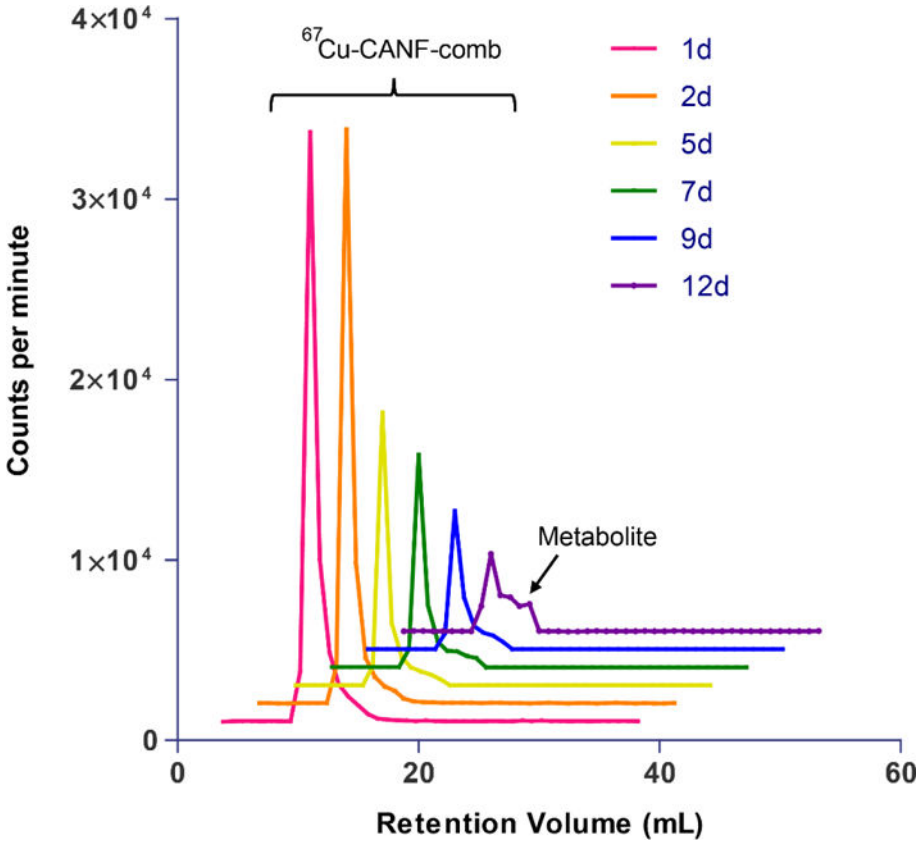

Fig. 6.

FPLC profiles of ^{67}Cu-CANF-comb in blood sampled from mouse at multiple time points post intravenous injection through tail vein.

Table 1

Characterization of Comb and 5 %, 10%, and 25% CANF-Comb

Polymer	M_n[a]	Đ[a]	Size (nm)[b]	ζ-Potential (mV)	# of CANF /nanoparticle[c]	# of DOTA/nanoparticle[c]	^{64}Cu radiolabeling specific activity (GBq/nmol)	Log P
Comb	220,000	1.25	22	−35 ± 2	N/A	105	4.5 ± 0.8	−2.5 ± 0.3
5% CANF-Comb	166,000	1.80	17	2.6 ± 3.7	7	105	1.4 ± 0.5	−2.1 ± 0.2
10% CANF-Comb	205,000	1.20	17	1.9 ± 3.4	14	105	5.4 ± 1.2	−2.0 ± 0.3
25% CANF-Comb	205,000	1.20	16	−1.1 ± 1	35	105	3.7 ± 1.1	−1.3 ± 0.4

[a] Determined by GPC in DMF, calibrated to PMMA standards ($gmol^{-1}$), Đ = M_w/M_n.

[b] Measured by dynamic light scattering.

[c] Predicted incorporation